Thermomechanical Characterization and Optimization of Liquid Crystal Elastomer Actuators Activated via Integrated Joule Heating

E. Chin[1], X. Liu[2], K. Sampson[2], I. Garcés[1*], and C. Paquet[2]

[1] Department of Mechanical and Aerospace Engineering, Carleton University, Ottawa, Canada,
[2] Quantum and Nanotechnologies Research Centre, National Research Council Canada, Ottawa, Canada

* *Corresponding author (IrinaGarces@cunet.carleton.ca)*

Keywords: *liquid crystal elastomers; soft actuators; Joule heating; smart materials; thermomechanical characterization*

1. Abstract

Liquid crystal elastomers (LCEs) are promising smart materials used for fabricating soft actuators capable of producing large, reversible deformations; however, their practical use is limited by their slow thermally driven response times in comparison to conventional actuating systems. In this work, nickel-chromium (NiCr) wires were embedded into mechanically programmed LCEs to produce Joule-heated actuators. The effects of the packing density of embedded NiCr wire and electrical power input parameters on actuation performance were investigated. Shape-memory programmed LCE samples were tested using three different embedded wire configurations (C1, C2, C3) under constant power inputs of 4.2, 5.7, and 7.0 W, as well as pulsed power inputs with duty cycles (DCs) of 30% and 60%, and pulse frequencies of 0.2, 0.5, 1.0, and 2.0 Hz. Actuation strain and velocity were quantified using digital image tracking, and thermal characterization was performed using differential scanning calorimetry and thermal imaging. Increased power input and embedded wire length increased the peak actuation velocity and reduced the times to reach peak velocity. Relative to a 4.2 W power input, increases of 36% (5.7 W) and 67% (7.0 W) increased peak actuation velocity by 40% and 87%, respectively, and reduced the times to peak velocity by 38% and 53%, respectively. Similarly, relative to an embedded wire length of 48 mm, increases of 15% and 48% increased peak actuation velocity by 23% and 61%, respectively, and reduced the times to peak velocity by 15% and 36%, respectively. In pulsed power input testing, higher DCs produced actuation responses closer to that of continuous heating while lower DCs enabled more gradual deformation. The unique capability of LCE actuators to be precisely velocity-controlled and held at intermediate, partially recovered strain states through modulated power input was demonstrated. These results show that the performance of Joule-heated LCE actuators can be tuned through both embedded conductor design and electrical input conditions, providing a foundation for engineering faster, more controllable, and more energy-efficient soft actuator systems.

2. Introduction

Conventional robotic and mechatronic systems rely on rigid actuators, electric motors, hydraulic pistons, and pneumatic drives that are effective for structured, high-force tasks but are poorly suited to applications requiring mechanical compliance, biological compatibility, or complex shape change [1], [2]. These systems cannot readily conform to irregular surfaces, safely

accommodate unexpected contact forces, or reproduce the continuous compliance of biological tissue, restricting their use in human-interactive, biologically integrated, and geometrically complex environments [1], [2]. Soft actuators, which generate motion through the controlled deformation of compliant materials rather than rigid mechanical linkages, address these limitations directly through their inherent ability to adapt to irregular surfaces of varying stiffness [1], [3]. In biomedical applications, these capabilities enable safe interaction with delicate biological tissue where rigid actuators are unsuitable, such as minimally invasive surgical tools and implantable devices [4], [5]. Additional applications include wearable assistive systems and prosthetics [6-8], bioinspired locomotion systems [9], [10], and morphing or deployable structures [11], [12].

Among soft actuator materials, liquid crystal elastomers (LCEs) are particularly attractive: they are lightweight, anisotropic polymer networks capable of large, reversible mechanical deformation in response to external stimuli, most commonly direct thermal activation or photothermal activation [13], [14]. Thermal actuation is widely used due to its straightforward implementation and direct coupling to the nematic-to-isotropic phase transition, during which liquid-crystalline mesogens reorient within the crosslinked elastomer network to produce macroscopic shape change [15], [16]. This molecular reorientation typically results in actuation stress outputs of ~0.3 MPa [17-19] and strain outputs of ~20-45% [11], [19], [20], comparable to that of biological skeletal muscle (~0.35 MPa, 20-30%) [21], [22]. These properties make LCEs promising candidates for soft actuation systems. More broadly, their programmable shape-morphing capability has enabled adaptive and reconfigurable structures in emerging areas such as 4D printing [16], [20], [23].

Despite these advantages, a critical and persistent limitation of thermally driven LCE actuators is their slow response velocity [24], [25]. Reported actuation times for thermally driven LCEs range from several to tens of seconds [24], [25], far slower than biological skeletal muscle, which contracts in less than 1 s [26], and than competing soft actuator technologies such as dielectric elastomers (< 0.5 s) [27], [28] and pneumatic artificial muscles under typical operating conditions (< 1 s) [29], [30]. These response times substantially limit the applicability of LCE actuators in time-sensitive domains [24]. The response time of thermally driven LCE actuators is primarily governed by the rate of bulk heat transfer through the material, with secondary contributions from viscoelastic polymer relaxation dynamics during phase transitions [25], [15], [31].

Thermally responsive LCE actuators have been successfully demonstrated across a range of geometries and configurations [9], [20]; however, most studies remain proof-of-concept and rely on bulk heating methods such as heat guns or thermal ovens to drive actuation [32], [33]. While suitable for material characterization, these approaches use externally controlled heating methods that are difficult to replicate in practical applications. Thus, actuation behaviour reported in such studies may not be representative of actuator performance in realistic operating environments [24].

Localized electrical heating via embedded conductive elements has been explored as a more practical alternative, enabling on-demand and spatially controlled thermal activation without requiring a heated enclosure or forced convection [34], [35]. However, existing studies that employ Joule heating in LCEs have not systematically investigated how heating parameters, such as embedded conductor density, power magnitude, or duty cycle (DC), influence actuation velocity and power efficiency.

Compounding these challenges, the thermal transport properties of LCEs remain incompletely characterized and are known to be anisotropic, varying with mesogen alignment, crosslinking density, molecular architecture (e.g., main-chain versus side-chain liquid crystalline networks), and temperature, all of which vary between LCEs or evolve during thermal actuation [36-39]. This complex coupling between structure and thermal transport complicates the prediction of heat transfer and actuation behaviour, limiting the current feasibility of purely computational design approaches [40], [41]. The lack of an established framework for the manufacturing and characterization of motion-controlled LCE actuators underscores the need for experimental studies that couple electrical, thermal, and mechanical responses under relevant operating conditions.

3. Materials and Methods

3.1. Sample preparation

LCE samples were made with base components of reactive mesogen RM257 as the mesogenic monomer, 2,2′-(ethylenedioxy)diethanethiol (EDDET) as the chain extender, pentaerythritol tetrakis(3-mercaptopropionate) (PETMP) as a crosslinker, and tetrahydrofuran (THF) as the solvent. Samples (n = 9) were fabricated with rectangular strip dimensions of ~30 × 3.5 × 2 mm. To program the actuation behaviour, the LCE samples were mechanically stretched to 100% strain at a velocity of 1 mm/s and subsequently ultraviolet (UV) cured in a *Formlabs* Form Cure L post-cure unit for 20 minutes with 405 nm light while maintained under strain. After programming, 40 AWG nickel-chromium (NiCr) wire (diameter = 0.08 mm) was mechanically embedded within LCE samples to act as high-resistance Joule heating elements. The total embedded NiCr wire length was varied between samples to examine the effects of heating density and spatial heat distribution. Samples (n = 3) of each wire configuration, named C1, C2, and C3, were fabricated, summarized in Table 1.

Table 1. Summary of parameters of wire configurations C1, C2, and C3 embedded into LCE samples.

Embedded Wire Pattern	Wire Configuration	Embedded Wire Length	Embedded Wire Length Increase Relative to C1	Dimension *A* (mm)	Dimension *B* (mm)
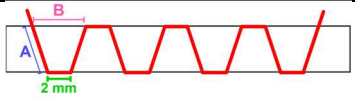	C1	48 ± 1 mm	0% (baseline)	3.75	4.7
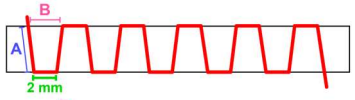	C2	55 ± 1 mm	15%	3.54	3.0
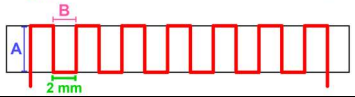	C3	71 ± 4 mm	48%	3.50	2.0

3.1. Thermal characterization

Differential scanning calorimetry (DSC) was performed to identify the nematic-isotropic transition temperature (T_{ni}) of the LCE using a *TA Instruments* DSC Q2000. A shape-memory programmed LCE sample with no embedded wire and a mass of 13 mg was analyzed over a temperature range of -20 °C to 140 °C at a heating and cooling rate of 10 °C/min. A modulation rate of 1 °C/min was applied, with 2 min isothermal holds at the maximum and minimum temperatures.

3.2. Thermal imaging

Thermal images of a C1 LCE sample were acquired using an *FLIR* Edge thermal camera to monitor thermal gradients during Joule heating-induced actuation at a constant power input of 4.2 W. Images were collected at 5, 10, 20, and 45 s after the onset of heating.

3.3. Characterization of thermomechanical actuation strain response

Joule heating of the embedded NiCr wire was generated using a *Keysight* E36312A DC power supply operated in constant-current (CC) mode. Secure electrical connections were established between the exposed NiCr wire and the power supply terminals. A total active resistive wire length of 200 ± 10 mm between the two electrical connection points was maintained across all samples. The power supply delivered either a constant current or a pre-programmed pulsed current with a specified duty cycle (DC) and cycle frequency.

Samples with wire configurations C1, C2, and C3 were evaluated under constant electrical power inputs of 4.2 ± 0.1 W, 5.7 ± 0.3 W, and 7.0 ± 0.5 W. The nine wire configuration-power combinations were each tested three times, with a different sample used in each trial (n = 27). The Joule-heated actuation response of an LCE sample with wire configuration C3 was evaluated under square-wave pulsed power excitation. Each DC condition (30% and 60%) was tested at pulse frequencies of 0.2, 0.5, 1.0, and 2.0 Hz, with a single trial conducted for each DC-frequency combination. During each pulse cycle, electrical power was set to 7.0 W during the high-power phase and 0 W during the low-power phase. Power input conditions for both DC cases (30%, 60%) are shown in Figure 1 at cycle frequencies of a) 0.2, b) 0.5, c) 1.0, and d) 2.0 Hz.

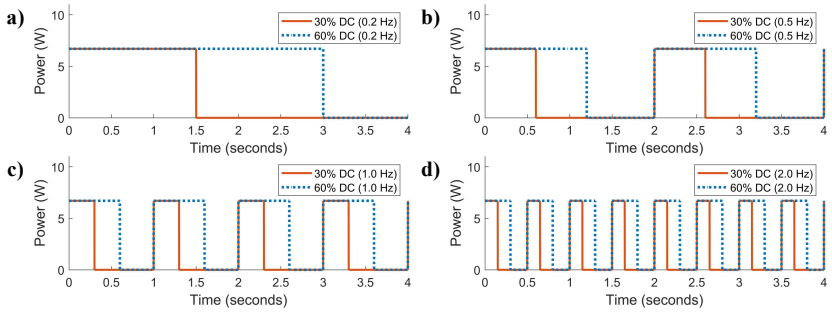

Figure 1. Power vs. time for DCs of 30% and 60% at cycle frequencies of a) 0.2 Hz, b) 0.5 Hz, c) 1.0 Hz, and d) 2.0 Hz.

Figure 2. LCE actuator sample Joule heating test setup.

3.4. Actuation strain image tracking

During Joule heating, sample deformation was recorded using a *TOMLOV* DM9 digital microscope (~5× magnification). The changes in length of LCE actuator samples were tracked using an active area of 10 ± 0.5 mm, marked by two white-coloured bands with black internal lines illustrated in Figure 2. A polytetrafluoroethylene (PTFE) sheet was placed underneath samples to minimize friction during actuation. One end of each sample was secured to the PTFE sheet to ensure stable positioning and improve tracking accuracy. Digital microscope video recordings (25 fps) of LCE sample actuation tests were analyzed using *Fiji* (*ImageJ*) by identifying the two marker lines and tracking the centroids of the two regions. Using *MATLAB*, the 2D Euclidean distance between marker centroids was computed for each frame, and the resulting displacement

data were smoothed using a Savitzky-Golay filter to reduce measurement noise. Actuation velocity was then calculated from frame-to-frame displacement. The velocity data were subsequently smoothed using a second Savitzky-Golay filter.

Percentage actuation strain recovery (%SR) was quantified as the percentage of the total programmed shape-memory strain that was recovered, as defined in Equation 1. Here, *recovered strain* represents the recovered strain in the active region at a given time, and *total programmed strain* is the strain imposed during shape-memory programming.

$$\%SR = \frac{recovered\ strain}{total\ programmed\ strain} \times 100\% \quad (1)$$

4. Results and Discussion

4.1. Differential scanning calorimetry

DSC analysis of the shape-memory programmed LCE revealed a reversible endothermic peak near 82 °C during heating, corresponding to the nematic-isotropic transition temperature (T_{ni}). A broad heat-flow peak was observed around T_{ni} = 82 °C, suggesting the transition occurs over a range of temperatures and a gradual rather than abrupt onset of actuation during heating.

4.2. Heating distribution

Thermal imaging of a C1 sample during Joule heating showed a gradual change in surface thermal distribution over time under a constant power input of 4.2 W, as shown in Figure 8. At activation times of 5, 10, and 20 s, heat was concentrated near the embedded wire, with increased temperatures near wire segments located close to or protruding from the sample surface. As the infrared camera measured surface temperature, exposed wire segments were imaged directly, resulting in higher recorded temperatures that reflected the wire temperature rather than the temperature of the surrounding sample surface. Nearly uniform heating was achieved by 45 s.

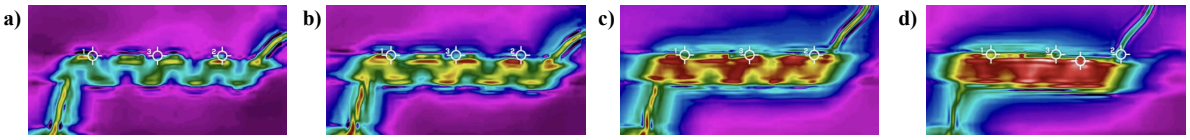

Figure 8. Thermal images of C1 sample at a) 5 s, b) 10 s, c) 20 s, and d) 45 s during heating at a constant power input of 4.2 W.

4.3. Thermal Actuation

The %SR of a C3 sample was tracked over three 7.0 W cycles to assess cyclic reversibility, shown in Figure 3. %SR remained consistent across cycles, attaining similar peak values each cycle.

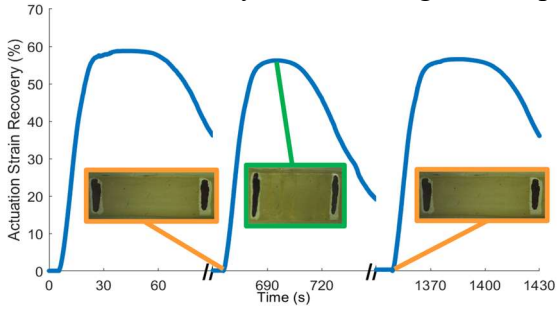

Figure 3. %SR vs. time for wire configuration C3 at a power level of 7.0 W for three heating-cooling actuation cycles, with images of the uncontracted and contracted sample taken before, during, and after actuation cycle.

The %SR and velocity for all constant-power tests were compared across wire configurations (C1, C2, C3) and power levels (4.2, 5.7, and 7.0 W), as shown in Figure 4. For each power level, the median response and minimum-maximum bounds are shown for the three wire configurations. Across all test conditions, the %SR remained below 70%, suggesting that the programming strain may have exceeded the soft elastic limit of the LCE network, at which point the polymer chains are stretched past their fully aligned state before the second (shape-memory programming) crosslinking step fixes the network in this strained configuration. In this condition, the actuator cannot fully recover the isotropic mesogen configuration upon heating, reducing the recoverable percentage actuation strain [43], [20].

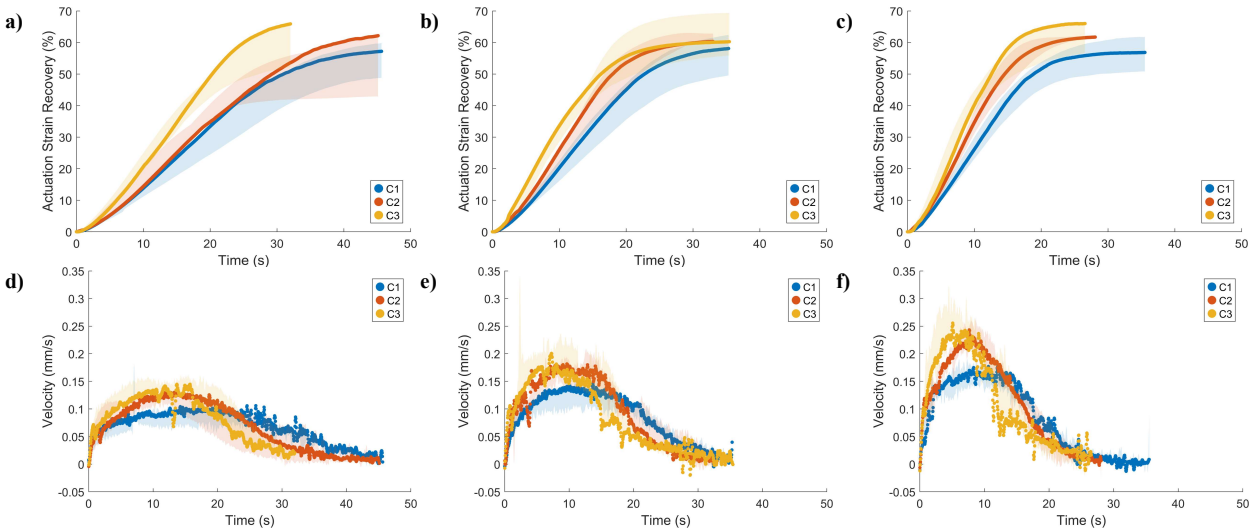

Figure 4. Median and shaded minimum-maximum %SR (top) and velocity (bottom) for each wire configuration at constant power levels of 4.2 W (left), 5.7 W (middle), and 7.0 W (right) (n = 3 for each curve).

Results indicate that increasing embedded wire length produces higher peak actuation velocities, shorter times to reach peak velocity, and earlier attainment of steady-state deformation. For example, at 7.0 W, median peak velocities were approximately 0.18 mm/s at 12 s, 0.24 mm/s at 8 s, and 0.30 mm/s at 5 s for samples C1, C2, and C3, respectively. Across all power levels (4.2, 5.7, and 7.0 W), C3 samples produced the highest peak velocities and the fastest times to peak velocity and to steady-state, indicating that increasing embedded wire length increases initial acceleration.

A similar trend was observed when comparing power levels for a given wire configuration. Increasing input power also resulted in faster peak actuation velocities, shorter times to reach peak velocity, and earlier attainment of steady-state deformation. The median C1 sample exhibited peak velocities of 0.11 mm/s at 16 s, 0.15 mm/s at 11 s, and 0.18 mm/s at 7 s for inputs of 4.2, 5.7, and 7.0 W, respectively. Across all wire configurations (C1-C3), the 7.0 W condition consistently produced the highest peak velocities and the fastest times to peak velocity and to steady-state.

Relative to the shortest embedded wire length of 48 mm, increasing the embedded wire length by 15% and 48% increased peak velocities by 23% and 61%, respectively, and reduced times to reach peak velocity by 15% and 36%, respectively. Similarly, relative to the lowest power level (4.2 W), power increases of 36% (5.7 W) and 67% (7.0 W) increased peak velocities by 40% and 87%, respectively, and decreased times to reach peak velocity by 38% and 53%, respectively.

These trends can be attributed to increased total Joule heating within the sample. Under current-controlled operation, increasing embedded wire length increases the total electrical resistance of the heating element ($R \propto L$), leading to higher total Joule heating power ($P = I^2R$). While local power dissipation per unit length remains approximately constant, the increased wire length results in a greater total thermal energy input and a more spatially distributed heating profile, reducing the time required to reach T_{ni}, contributing to faster actuation. However, embedded wires can add an additional stiffness to the material's system that could contribute to actuation behaviour. Furthermore, they may disrupt polymer chain alignment or inhibit their spatial reordering during actuation. Overall, these results indicate that tuning both electrical power input magnitude and embedded wire length enables optimization and tailoring of actuation velocity and response time.

4.4. Power duty cycle testing

Figure 5 shows the %SR over time for the four pulse frequencies (0.2, 0.5, 1.0, 2.0 Hz), with responses for each DC condition (30, 60, 100%) shown. The pulsed power input profile for the 0.2 Hz 30% DC condition is included for reference. Results showed that 60% DC condition reduced power input by 40% from the continuous condition but exhibited only slightly slower actuation than continuous heating (100% DC), while the 30% DC condition resulted in significantly slower actuation than 60% DC. This suggests diminishing gains in actuation performance at higher DCs.

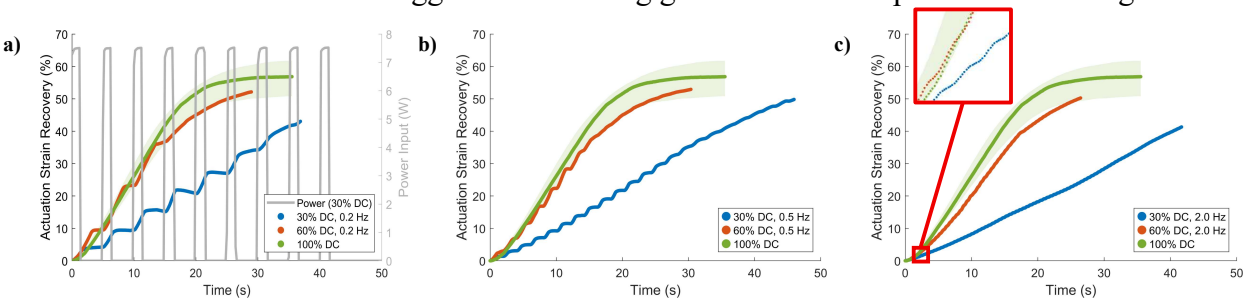

Figure 5. %SR achieved by C3 sample during 7.0 W activation with DCs of 30%, 60 %, and 100% at cycle frequencies of a) 0.2 Hz, b) 0.5 Hz, and c) 2.0 Hz.

When the pulsed power data were regrouped by DC, such that responses at 0.2, 0.5, 1.0, and 2.0 Hz were compared within each DC condition, frequency was found to have little influence on total actuation time. The spread in %SR across frequencies was relatively small for both the pulsed power conditions (30%, 60%). 60% DC tests exhibited particularly little variation across frequencies, while 30% DC tests showed a larger spread, suggesting a greater sensitivity to frequency at lower DC. This broader spread across frequencies can likely be attributed to longer LCE cooling intervals at lower DC, allowing more thermal actuation relaxation between cycles. In contrast, the 60% DC samples retained more heat between cycles, allowing %SR to be more effectively maintained between pulses and reducing frequency-dependent variation in actuation behaviour. Additionally, the lower DC (30%) produced a more uniform and gradual %SR over time, exhibiting closer to a linear trend compared to the 60% and 100% DC, which may be advantageous in applications requiring more constant or predictable actuation. Higher cycle frequencies, and thus shorter pulse and cycle durations, appeared to correlate with slightly slower overall actuation, most noticeably in the 30% DC tests. At higher frequencies, the LCE does not have sufficient time to fully develop its thermomechanical response within each cycle, and the system instead responds to an effective average power input.

Although the 2.0 Hz tests exhibited reduced %SR during the low-power portions of the cycle, resulting in a smoother overall actuation profile, periodic modulation associated with the alternating of heating and cooling occurring every 0.5 s (Figure 5c) was still observed. This indicates that the actuator response occurred on timescales comparable to the 0.5 s cycle period. In contrast, the 0.2 Hz tests displayed much larger peaks and troughs in the actuation profile over time due to longer heating and cooling intervals. The 0.2, 0.5, 1.0, and 2.0 Hz tests reached 50% SR at approximately 45, 46, 48, and 50 s, respectively.

Figure 6 shows the %SR in the C3 sample during a 7.0 W input at cycle frequencies of 0.2, 0.5, 1.0, and 2.0 Hz with DCs of 30% and 60%; the pulsed power input profile for the 0.2 Hz 30% DC condition is shown in Figure 6a for reference.

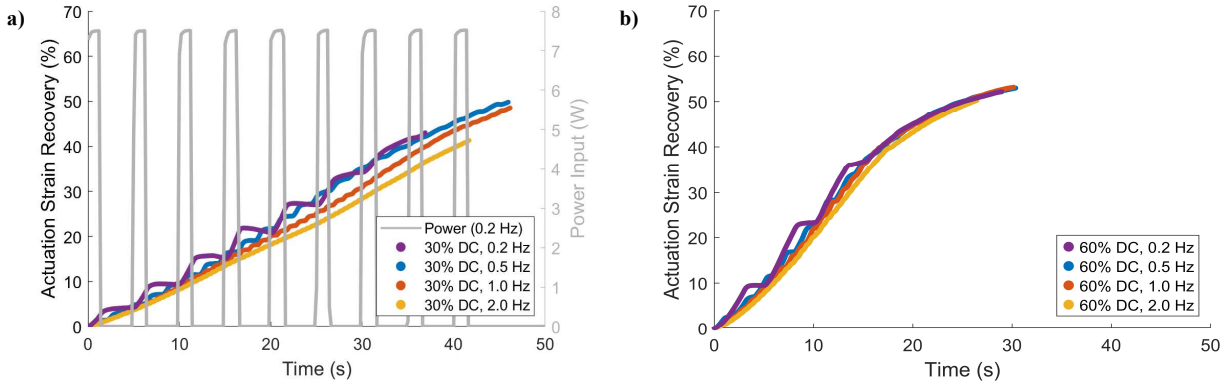

Figure 6. %SR in C3 sample during 7.0 W input at cycle frequencies of 0.2, 0.5, 1.0, and 2.0 Hz with DCs of a) 30% and b) 60%.

Peak actuation velocity decreased with increasing cycle frequency. Figure 7 shows the actuation velocity of the C3 sample with a 7.0 W input at frequencies of a) 0.2, b) 0.5, c) 1.0, and d) 2.0 Hz with 30, 60, and 100% DCs; the power input profile for the 0.2 Hz 30% DC condition is shown in Figure 7a for reference. At 0.2 Hz, the 30% DC produced the highest peak actuation velocity despite its peak arriving later than those of the 60% and 100% conditions. A likely explanation is that the bulk material temperature remains partially heated between pulses, allowing the LCE to begin subsequent pulses from a higher thermal baseline, thus crossing T_{ni} more rapidly and producing a faster peak contraction rate. The 100% DC condition produced steadier and more continuous actuation with fewer velocity spikes.

At higher frequencies (0.5, 1.0, and 2.0 Hz), the 30% DC produced lower peak actuation velocities than the 60% DC but outperformed the 100% DC at the lowest frequency (0.2 Hz). This result suggests a transition from discrete pulse-dominated behaviour to an averaged thermal response regime as frequency increases. The change in ranking of peak actuator velocity between 0.5 and 1.0 Hz suggests that the actuator's characteristic thermal time constant lies within this range, above which pulsed and continuous heating produce increasingly similar thermomechanical responses.

During low-power intervals between successive 7.0 W pulses, periods of near-zero velocity were observed in all cases while some small negative velocities, most notably at 0.2 Hz (Figure 7a), indicated partial relaxation toward the nematic state. These results demonstrate that pulsed power parameters can be used to systematically tune the actuation behaviour of LCE-based Joule-heated actuators.

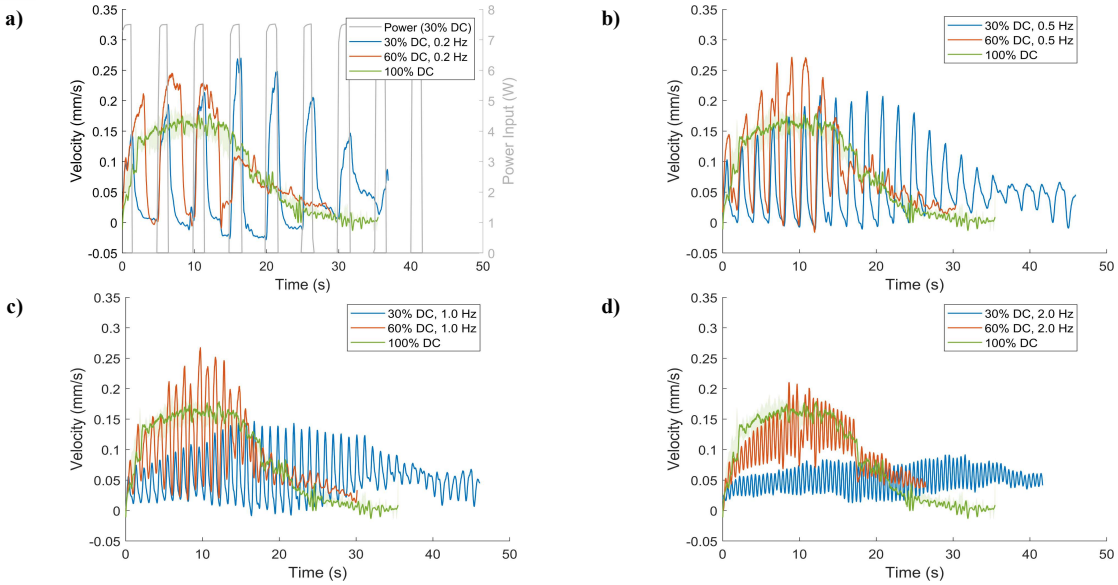

Figure 7. Actuation velocity of C3 sample during 7.0 W pulsed operation at cycle frequencies of a) 0.2 Hz, b) 0.5 Hz, c) 1.0 Hz, d) 2.0 Hz shown for DCs of 30%, 60%, and 100%.

4.5. Motion control of LCEs

Pulsed power input for Joule-heated LCE actuators enables tunable and more controllable actuation behaviour compared to continuous heating, allowing precise control over actuation velocity, strain rate, and thermal distribution. By adjusting DC and frequency, the potential to modulate actuation in real time was demonstrated, including the ability to slow, accelerate, or halt motion at intermediate partial strain states – capabilities not typically achievable in most shape memory polymers, which generally exhibit binary "on/off" actuation.

Increasing DC increases heat retention, resulting in smoother and more continuous deformation, improved strain maintenance, and reduced power requirements to achieve comparable %SR and velocity. In contrast, lower DCs slow actuation but promote thermal relaxation between pulses, supporting more uniform heat distribution, homogeneous mesogen reorientation, and coordinated actuation. Frequency further governs actuation dynamics by controlling the extent of thermal recovery between pulses. In this work, the LCE remained responsive at the highest tested frequency of 2.0 Hz, suggesting rapid actuation dynamics on sub-second timescales.

5. Conclusions

This study demonstrated that the performance of Joule-heated LCE actuators is governed by coupled electrical, thermal, and geometric effects. Increasing input power and embedded wire length increased actuation velocity. Pulsed power testing showed that DC and frequency govern the trade-off between velocity, strain stability, and thermal uniformity. Lower DCs and frequencies reduced velocity but enabled more gradual, near-linear actuation and improved %SR retention. The observed frequency-dependent response suggests a characteristic thermal time constant governs the transition between transient and steady-state behaviour. The results demonstrate potential for tuning and intermittently halting LCE actuation through modulation of electrical input signal. Further development and characterization of motion-controlled LCEs is currently ongoing.

6. References

[1] D. Rus and M. T. Tolley, "Design, fabrication and control of soft robots," Nature, vol. 521, no. 7553, pp. 467–475, 2015.
[2] C. Laschi, B. Mazzolai, and M. Cianchetti, "Soft robotics: Technologies and systems pushing the boundaries of robot abilities," Sci. Robot., vol. 1, no. 1, eaah3690, 2016.
[3] G. M. Whitesides, "Soft-Robotik," Angew. Chem., vol. 130, no. 16, pp. 4336–4353, 2018.
[4] C. P. Ambulo et al., "Processing advances in liquid crystal elastomers provide a path to biomedical applications," J. Appl. Phys., vol. 128, 140901, 2020.
[5] S. Tasmim et al., "Liquid crystal elastomer based dynamic device for urethral support: Potential treatment for stress urinary incontinence," Biomaterials, vol. 292, 121912, 2023.
[6] S. I. Rich, R. J. Wood, and C. Majidi, "Untethered soft robotics," Nat. Rev. Mater., 2018.
[7] C.-Y. Chu and R. M. Patterson, "Soft robotic devices for hand rehabilitation and assistance: A narrative review," J. Neuroeng. Rehabil., vol. 15, 9, 2018.
[8] M. Li et al., "Soft actuators for real-world applications," Nat. Rev. Mater., vol. 7, pp. 235–249, 2022.
[9] T. Zang et al., "State of the Art, Insights and Perspectives for Bio-Inspired Liquid Crystal Elastomer Soft Actuators," Adv. Mater., 2025.
[10] B. Lei et al., "Bioinspired Jumping Soft Actuators of the Liquid Crystal Elastomer Enabled by Photo-Mechanical Coupling," ACS Appl. Mater. Interfaces, vol. 16, 1596–1604, 2024.
[11] F. Wang et al., "4D printing of carbon-fiber-reinforced liquid crystal elastomers for self-deployable solar panels," Mater. Horiz., vol. 12, pp. 5315–5324, 2025.
[12] A. F. Minori et al., "Reversible actuation for self-folding modular machines using liquid crystal elastomer," Smart Mater. Struct., vol. 29, 105006, 2020.
[13] Y. Deng and M.-H. Li, "Electroactive LCEs as soft actuators," Adv. Funct. Mater., vol. 36, e18797, 2026.
[14] J. P. F. Lagerwall, "Liquid crystal elastomer actuators and sensors: Glimpses of the past, the present and perhaps the future," Programmable Mater., vol. 1, 2023.
[15] A. R. Tajbakhsh and E. M. Terentjev, "Spontaneous thermal expansion of nematic elastomers," Eur. Phys. J. E, vol. 6, pp. 181–188, 2001.
[16] M. Chen et al., "Recent Advances in 4D Printing of Liquid Crystal Elastomers," Adv. Mater., 2023.
[17] H. Zhang et al., "Wireless Power Transfer to Electrothermal Liquid Crystal Elastomer Actuators," ACS Appl. Mater. Interfaces, vol. 15, pp. 27195–27205, 2023.
[18] D. J. Roach et al., "Novel ink for ambient condition printing of liquid crystal elastomers for 4D printing," Smart Mater. Struct., vol. 27, 125010, 2018.
[19] J. Min et al., "Intelligent Liquid Crystal Elastomer Actuators with High Mechanical Strength, Self-Sensing, and Automatic Control," Adv. Sens. Res., vol. 3, 2300117, 2024.
[20] R. Mouhoubi, V. Lapinte, and S. Blanquer, "DLP 4D Printing of Programmable Molecularly-Engineered Liquid Crystal Elastomer Actuators," Adv. Sci., 2026.
[21] L. S. Persad et al., "Specific tension of human muscle in vivo: a systematic review," J. Appl. Physiol., vol. 137, pp. 945–962, 2024.
[22] T. Mirfakhrai, J. D. W. Madden, and R. H. Baughman, "Polymer artificial muscles," Mater. Today, vol. 10, pp. 30–38, 2007.
[23] P. Mainik et al., "DLP 4D Printing of Multi-Responsive Bilayered Structures," Adv. Mater. Technol., vol. 8, 2023.
[24] J. M. Speregen and T. J. White, "Liquid Crystalline Elastomers in Soft Robotics: Assessing Promise and Limitations," 2025.
[25] C. Liu et al., "Achieving rapid actuation in LCEs," Natl. Sci. Open, 2025.
[26] R. J. Full and K. Meijer, "Metrics of natural muscle function," in Electroactive Polymer (EAP) Actuators, 2001, pp. 73–87.
[27] R. Pelrine et al., "High-field deformation of elastomeric dielectrics," Mater. Sci. Eng. C, vol. 11, pp. 89–100, 2000.
[28] K. Jia, T. Lu, and T. J. Wang, "Response time and dynamic range for a dielectric elastomer actuator," Sens. Actuators A, vol. 239, pp. 8–17, 2016.
[29] F. Daerden et al., "Pneumatic Artificial Muscles: actuators for robotics and automation," in Proc. IEEE/ASME AIM, 2002, pp. 738–743.
[30] B. Tondu, "Modelling of the McKibben artificial muscle: A review," J. Intell. Mater. Syst. Struct., vol. 23, pp. 225–253, 2012.
[31] F. Elias et al., "Equilibrium textures in main-chain liquid crystalline polymers," Europhys. Lett., vol. 47, pp. 442–447, 1999.
[32] H. Kim et al., "Effects of chain extender and crosslinking density of liquid crystal elastomers used in sequential actuators," Sens. Actuators B, vol. 450, 139241, 2026.
[33] S. Li et al., "Digital light processing of liquid crystal elastomers for self-sensing artificial muscles," Science, 2021.
[34] J. H. Lee et al., "Robust and Reprocessable Artificial Muscles Based on Liquid Crystal Elastomers with Dynamic Thiourea Bonds," Adv. Funct. Mater., vol. 32, 2022.
[35] J. Forman et al., "FibeRobo: Fabricating 4D Fiber Interfaces by Continuous Drawing of Temperature Tunable Liquid Crystal Elastomers," in Proc. UIST '23, 2023.
[36] Y. Cang et al., "On the origin of elasticity and heat conduction anisotropy of liquid crystal elastomers at gigahertz frequencies," Nat. Commun., vol. 13, 5000, 2022.
[37] Z. Li and Y. Liu, "The effect of crosslinking rate on the thermal and mechanical properties of liquid crystal elastomer: A molecular dynamics study," Mater. Today Commun., vol. 40, 110201, 2024.
[38] M. Wang et al., "Homeotropically-aligned main-chain and side-on liquid crystalline elastomer films with high anisotropic thermal conductivities," Chem. Commun., vol. 52, pp. 4313–4316, 2016.
[39] J. Shin et al., "Thermally Functional Liquid Crystal Networks by Magnetic Field Driven Molecular Orientation," ACS Macro Lett., vol. 5, pp. 955–960, 2016.
[40] Z. Wei, P. Wang, and R. Bai, "Thermomechanical Coupling in Polydomain Liquid Crystal Elastomers," J. Appl. Mech., vol. 91, 2023.
[41] A. E. H. Chehade et al., "Finite element modeling of viscoelastic liquid crystal elastomers," Int. J. Numer. Methods Eng., vol. 125, no. 16, 2024.
[42] C. M. Yakacki et al., "Tailorable and programmable liquid-crystalline elastomers using a two-stage thiol-acrylate reaction," RSC Adv., vol. 5, pp. 18997–19001, 2015.
[43] M. Barnes and J. S. Biggins, "Microstructural Basis of Complex Mechanical Programming in Liquid Crystal Elastomers," J. Elast., vol. 157, 2025, doi: 10.1007/s10659-025-10138-4.